

Relating Andreev Bound States and Supercurrents in Hybrid Josephson Junctions

F. Nichele,^{1,2,*} E. Portolés,¹ A. Fornieri,¹ A. M. Whiticar,¹ A. C. C. Drachmann,¹ S. Gronin,^{4,7} T. Wang,^{3,4} G. C. Gardner,^{4,7} C. Thomas,^{3,4} A. T. Hatke,^{3,4} M. J. Manfra,^{3,4,5,6,7} and C. M. Marcus^{1,†}

¹Center for Quantum Devices and Microsoft Quantum Lab—Copenhagen, Niels Bohr Institute, University of Copenhagen, Universitetsparken 5, 2100 Copenhagen, Denmark

²IBM Research—Zurich, Säumerstrasse 4, 8803 Rüschlikon, Switzerland


³Department of Physics and Astronomy, Purdue University, West Lafayette, Indiana 47907, USA

⁴Birk Nanotechnology Center, Purdue University, West Lafayette, Indiana 47907, USA

⁵School of Materials Engineering, Purdue University, West Lafayette, Indiana 47907, USA

⁶School of Electrical and Computer Engineering, Purdue University, West Lafayette, Indiana 47907, USA

⁷Microsoft Quantum Purdue, Purdue University, West Lafayette, Indiana 47907, USA

 (Received 18 December 2019; revised manuscript received 3 March 2020; accepted 27 April 2020; published 4 June 2020)

We demonstrate concomitant measurement of phase-dependent critical current and Andreev bound state spectrum in a highly transmissive InAs Josephson junction embedded in a dc superconducting quantum interference device (SQUID). Tunneling spectroscopy reveals Andreev bound states with near unity transmission probability. A nonsinusoidal current-phase relation is derived from the Andreev spectrum, showing excellent agreement with the one extracted from the SQUID critical current. Both measurements are reconciled within a short junction model where multiple Andreev bound states, with various transmission probabilities, contribute to the entire supercurrent flowing in the junction.

DOI: [10.1103/PhysRevLett.124.226801](https://doi.org/10.1103/PhysRevLett.124.226801)

Josephson junctions (JJs) in superconductor-semiconductor hybrids are objects of intense study. Electrostatic tuning of the critical current enables voltage controlled superconducting qubits [1–5]. Ballistic electron motion and spin-orbit interaction allow unique functionalities, such as spin-dependent supercurrents [6] and anomalous current-phase relation (CPR) [7–10]. Most remarkably, Andreev bound state (ABS) manipulation via phase biasing and Zeeman fields might stabilize electronic phases with topological protection [11–15]. Several studies characterized hybrid JJs in terms of CPR [16–19], however, critical current alone does not offer direct information of the ABS spectrum. On the other hand, ABS spectroscopy requires either weakly coupled tunneling probes or microwave spectroscopy techniques, both challenging to combine with standard transport measurements. As a result, direct visualization of ABSs could only be achieved for a limited selection of material systems, such as atomic break junctions [20], carbon nanotubes [21], graphene [22], and semiconductor nanowires [23,24], and not in combination with supercurrent measurements.

In this Letter, we investigate superconducting quantum interference devices consisting of two highly transmissive Josephson junctions coupled by a superconducting loop, all defined in an epitaxial InAs/Al heterostructure. A novel device design allows for independent measurements of the current-phase relation of one of the two junctions and the Andreev bound state spectrum within its normal region. Both measurements are reconciled within the short junction

model, where Andreev bound states with various transmission probabilities contribute to the entire supercurrent flowing in the junction. Quantitative understanding of field-dependent spectrum and supercurrent require taking into account the second junction in the loop and the kinetic inductance of the epitaxial Al film. This Letter highlights hybrid planar JJs as ideal test grounds for emerging paradigms in condensed matter physics, such as ABS manipulation in highly transmitting devices [25,26] and phase-tuned topology in multiterminal geometries [27–29].

Planar JJs were defined in an InAs quantum well contacted by a thin epitaxial Al film grown *in situ* [30,31]. Further details on the wafer structure are reported in the Supplemental Material [32]. Two lateral InAs regions covered by epitaxial Al constitute the superconducting leads, while the normal region is defined by selectively removing a stripe of epitaxial Al, exposing the semiconductor underneath. An energy diagram of the JJ under study is depicted in Fig. 1(a). The strong superconductor-semiconductor coupling in the leads results in an induced superconducting DOS with gap Δ^* , only slightly lower than the Al gap Δ [36]. For a JJ much shorter than the superconducting coherence length, a well-known relation exists between the energy E_i of an ABS and the phase difference between superconducting leads φ [37]

$$E_i(\varphi) = \pm \Delta^* \sqrt{1 - \tau_i [\sin(\varphi/2)]^2}, \quad (1)$$

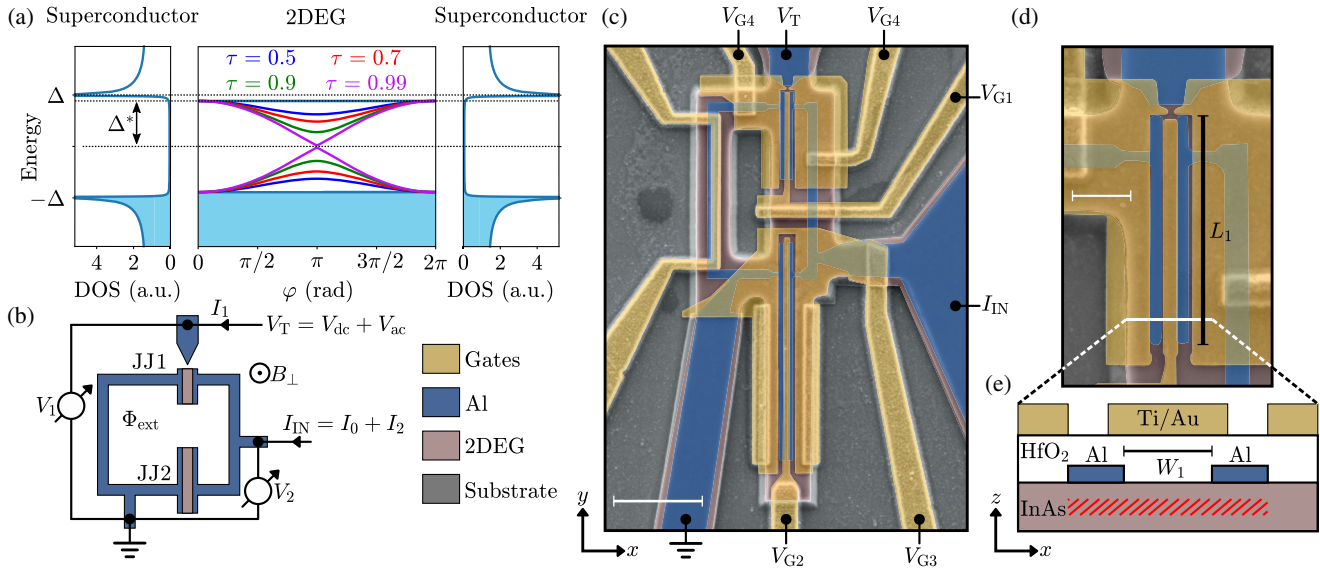


FIG. 1. (a) Schematic representation of the energy spectrum of a planar JJ. Two superconducting leads with a BCS-like DOS and induced gap Δ^* laterally confine a normal region in the 2DEG, in which discrete ABSs form within the induced superconducting gap. (b) Schematic representation of the device under study and its measurement setup. (c) False-color scanning electron micrograph of the device under study. The insulating substrate is gray, the semiconductor is red, and the thin Al film is blue. Top gates, colored yellow, were deposited over an insulating HfO_2 layer (not visible). A metallic strip line, not used in this Letter, was deposited on the left-hand side of the loop. Scale bar is $2 \mu\text{m}$. (d) Enlargement close to JJ1. A central top gate tuned the density in the normal region of JJ1, two additional top gates confined electrons below the superconducting leads and electrostatically defined a tunneling constriction between the normal region of JJ1 and a superconducting plane. Scale bar (white) is 500 nm . (e) Schematic cross section of JJ1. A negative gate voltage applied to the lateral gates depleted lateral InAs regions, leaving a conducting electron layer solely below the Al contacts and within the normal region of JJ1.

where τ_i is the transmission probability. The spectrum is periodic in φ and approaches zero energy for $\tau_i \rightarrow 1$ and $\varphi = \pi$. Each populated ABSs carries a supercurrent

$$I_i(\varphi) = -\frac{2e}{h} \frac{\partial E_i}{\partial \varphi}. \quad (2)$$

Summing the current contribution of all ABSs results in the CPR of the junction, so that a junction with highly transmissive modes is characterized by a forward-skewed sinelike CPR.

Phase tuning was achieved by embedding the junction of interest, referred to as JJ1, in a superconducting loop (also made of epitaxial Al on InAs) together with a second InAs/Al JJ, named JJ2. Dimensions were chosen so that the critical current of JJ2 (I_{C2}) was much larger than that of JJ1 (I_{C1}). A superconducting tunneling probe with tunable transmission was integrated laterally to JJ1, allowing spectroscopy. Figure 1(b) shows a schematics of the device, while a false-colored scanning electron micrograph is shown in Fig. 1(c). Figure 1(d) shows an enlargement of JJ1 and the tunneling probe.

The device, shown in Fig. 1(c), was defined by wet etching of the superconductor-semiconductor stack down to the insulating substrate. The epitaxial Al film was locally removed in order to form the normal regions of JJ1, JJ2,

and the tunneling probe. The sample was subsequently covered by a 18 nm thin film of insulating HfO_2 and patterned with top gates. Junctions had dimensions $W_1 = 80 \text{ nm}$, $L_1 = 1.6 \mu\text{m}$, $W_2 = 40 \text{ nm}$, and $L_2 = 5 \mu\text{m}$, where W is the separation between leads and L is their length [see Figs. 1(d) and 1(e)]. The loop was defined by a 160 nm wide epitaxial Al stripe and encloses an area of $7 \mu\text{m}^2$. Electrodes separation W_1 and W_2 are both significantly shorter than the superconducting coherence length in InAs, calculated as $\xi_S = \sqrt{\hbar v_F l / (2\Delta^*)} \sim 0.8 \mu\text{m}$, where v_F is the Fermi velocity and l is the elastic mean free path, setting both JJ1 and JJ2 in the short junction limit.

If not explicitly stated, the device was operated with gate voltages $V_{G1} = V_{G2} = 0$. Additional gates, set to negative voltages, laterally confine electrons underneath the Al leads. For JJ2, this is achieved with gate G_3 , while for JJ1 it is achieved with two gates that also define a constriction in the 2DEG and are operated at the same gate voltage V_{G3} . This concept is presented in Fig. 1(e), showing a cross section of JJ1 with the resulting conducting InAs region indicated by the shaded red area.

Devices were measured in a dilution refrigerator at a base temperature of 30 mK by low-frequency lock-in techniques. The measurement setup is schematically shown in Fig. 1(b). The tunneling differential conductance dI_1/dV_1 was measured by applying a voltage bias $V_T = V_{\text{dc}} + V_{\text{ac}}$

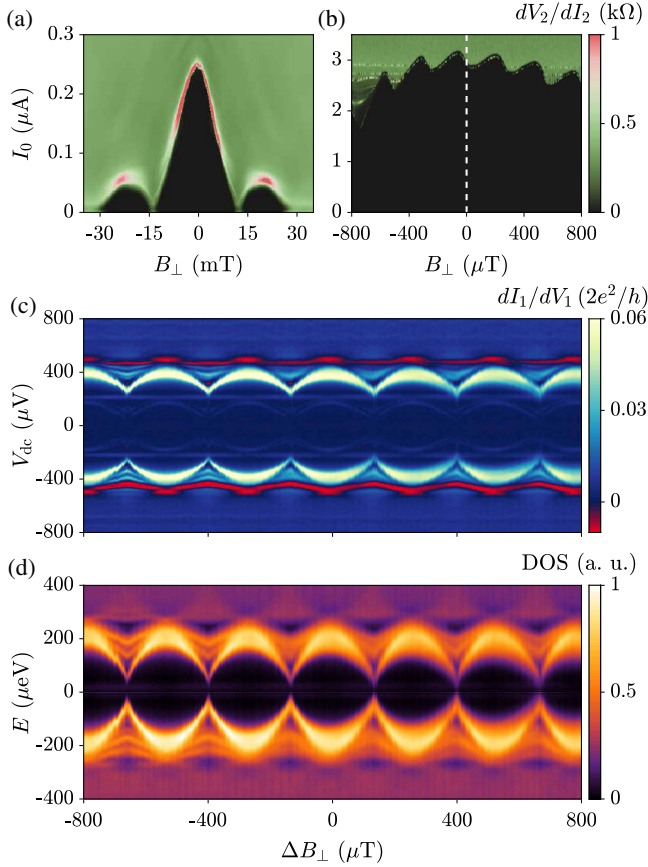


FIG. 2. (a) Loop resistance dV_2/dI_2 as a function of out-of-plane magnetic field B_\perp and dc current I_0 . Gate voltage V_{G2} was set to -3 V, so that a current can only flow in JJ1. (b) As in (a), but with the supercurrent flowing in both junctions. Notice the different magnetic field scale, highlighting supercurrent oscillations with a characteristic period consistent with one flux quantum impinging the loop area. The vertical dashed line marks the point with zero external magnetic field B_\perp . (c) Tunneling conductance dI_1/dV_1 as a function of bias voltage V_{dc} , measured for the same magnetic field range as in (b). (d) Density of states within the normal region of JJ1, computed from the data in (c) using a deconvolution algorithm.

to the tunneling probe via a low-impedance IV converter and recording the resulting current I_1 and differential voltage V_1 (where V_{dc} was a dc signal and V_{ac} , V_1 , and I_1 had frequency f_1). The loop differential resistance dV_2/dI_2 was obtained by injecting a current $I_{IN} = I_0 + I_2$ in the loop and recording the differential voltage V_2 (where I_0 was a dc signal and I_2 and V_2 had frequency f_2). Measurements shown here were obtained with $I_2 = 2$ nA, $V_{ac} = 3$ μ V, $f_1 = 131$ Hz, and $f_2 = 113$ Hz.

Figure 2(a) shows the loop resistance dV_2/dI_2 as a function of out-of-plane magnetic field B_\perp and I_0 for $V_{G2} = -3$ V, a situation in which JJ2 was closed and the current entirely flowed through JJ1. The critical current showed a Fraunhofer-like pattern, with maximum $I_{C1} = 240$ nA and zeros for $B_\perp = \pm 14$ mT, consistent with one

flux quantum $\Phi_0 = h/(2e)$ impinging through the normal region of JJ1. Setting $V_{G2} = 0$ allowed the current to flow in both junctions. In this gate configuration, the critical current had mean value $I_{C2} = 2.9$ μ A and was periodically modulated as a function of B_\perp [see Fig. 2(b)]. The modulation had amplitude I_{C1} and periodicity 265 μ T, consistent with magnetic flux quanta impinging through the superconducting quantum interference device (SQUID) loop. The dashed vertical line in Fig. 2(b) marks the position of $B_\perp = 0$, carefully measured as described in the Supplemental Material [32]. In this unbalanced SQUID regime ($I_{C2}/I_{C1} = 12$), the critical current modulations are reminiscent of the CPR of JJ1 [19], as discussed below.

The tunneling differential conductance dI_1/dV_1 , measured in the same regime as in Fig. 2(b), is shown in Fig. 2(c). Consistent with a superconductor-insulator-superconductor junction, data showed a transport gap within $V_{dc} = \pm 2\Delta^*/e \approx 400$ μ V and regions of negative differential conductance [38]. The energy spectrum of JJ1, shown in Fig. 2(d), was obtained by applying the deconvolution algorithm described in Refs. [21,32] to the data of Fig. 2(c). For this procedure, we assumed the tunneling probe was characterized by a superconducting DOS with gap $\Delta^* = 200$ μ eV and Dynes parameter $\gamma = 0.02$, as in measurements performed on similar heterostructures [31,38]. The deconvolved DOS displays a gap $\Delta^* = 200$ μ eV in which discrete and periodically modulated ABSs coexist. Some approach zero energy, indicating very high transmission, while others, with lower transmission, evolve closer to the gap edge.

The derived DOS was then used to compute the field-dependent supercurrent as the sum of the contributions of each occupied ABS ($E_i < 0$), as per Eq. (2). Here we used the approximation

$$I_1(\varphi_1) = -\frac{2e}{h} \sum_i \frac{\partial E_i}{\partial \varphi_1} \approx -\frac{2e}{h} \int_E \frac{\partial D}{\partial \varphi_1} \epsilon d\epsilon; \quad (3)$$

that is, we substituted the summation with an integral of the phase derivative of the DOS D times energy, which is readily computed on the data of Fig. 2(d). Figure 3(a) compares the field-dependent supercurrent of JJ1 extracted from the critical current modulation of Fig. 2(b) [39] (blue dots) and that numerically derived from the ABSs of Fig. 2(c) and Eq. (3) (green line). The matching of the two curves is striking, confirming that, indeed, the CPR of JJ1 is completely determined by its ABS spectrum. Furthermore, the pronounced forward skewness indicates a high effective transmission. Points extracted from the critical current (blue dots) were shifted by 170 μ T with respect to the magnetic field they were measured at [the vertical blue marker indicates the position where $B_\perp = 0$ was identified in Fig. 2(b)]. As discussed in the following, the shift is due to current-induced magnetic fluxes induced within the device and is accounted for by our model.

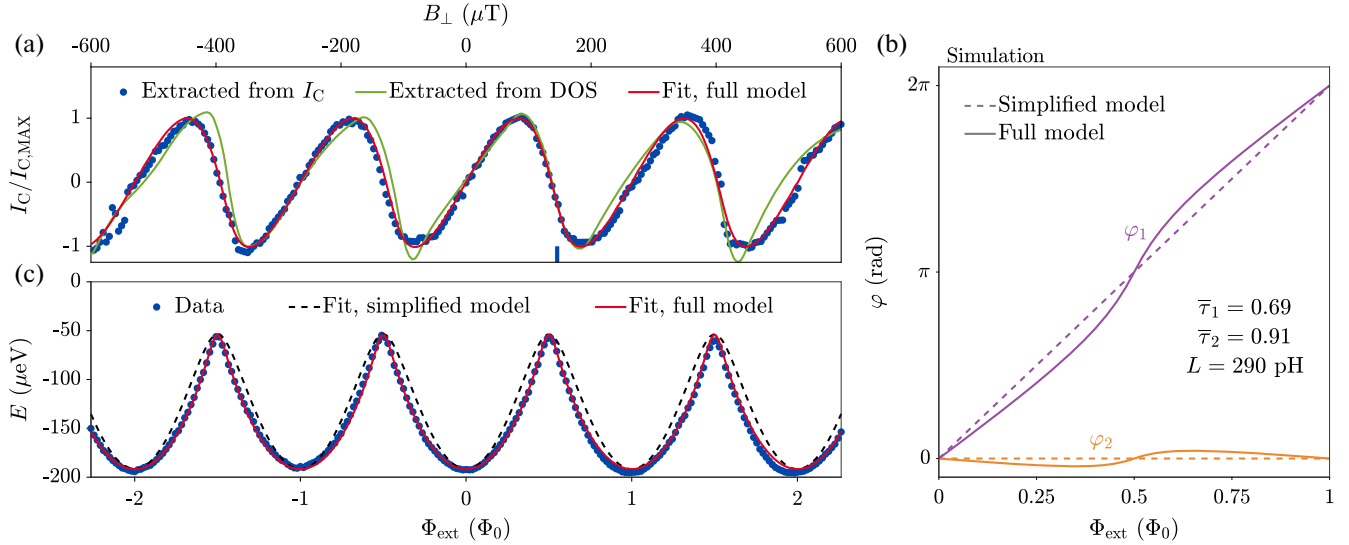


FIG. 3. (a) SQUID critical current as a function of out-of-plane magnetic field B_{\perp} [blue dots, extracted from Fig. 2(b)] together with the critical current calculated based on the data in Fig. 2(d) (green) and a fit to the full numerical model (red). The fit used the effective transmissions $\bar{\tau}_1$ and $\bar{\tau}_2$ as free parameters. Blue data points have been horizontally shifted by $170 \mu\text{T}$ in order to match the other curves. The vertical blue marker shows the position where $B_{\perp} = 0$ occurred in the raw data. (b) Phase differences φ_1 and φ_2 across JJ1 and JJ2, respectively. Dashed lines refer to the simplified model, which considers $I_C2 \gg I_C1$ and no loop inductance. Solid lines are calculated using our full model and the fit result of (a). (c) Energy of the most transmissive ABS visible in Fig. 2(d) (blue dots) together with a fit to Eq. (1) that includes the nonlinear mapping between Φ_{ext} and φ_1 shown in (b) (red line). The dashed black line is a fit to Eq. (1) using the simplified assumption $\varphi_1 = 2\pi\Phi_{\text{ext}}$. In this case, the fit was forced to match the data in the points of highest energy.

In a first simplified approximation, an external flux Φ_{ext} through the loop results in a phase difference $\varphi_1 \approx 2\pi\Phi_{\text{ext}}$ across JJ1, while the phase difference φ_2 across JJ2 remains zero, as shown by dashed lines in Fig. 3(b). However, in the present case, two complications arise. First, JJ1 is in parallel with a second highly transmissive JJ, which introduces a nonlinear Josephson inductance. Second, the epitaxial Al used for the superconducting loop is particularly thin, resulting in a finite kinetic inductance $L_K \approx 290 \text{ pH}$ [32]. In this framework, the effective flux Φ impinging through the loop is the difference between the externally applied flux Φ_{ext} and the current induced flux $L_K(I_2 - I_1)/2$. The JJs are both in the ballistic regime, resulting in nonsinusoidal CPRs. We describe the CPR of each junction using Eq. (2), where τ of Eq. (1) is substituted with an effective transmission $\bar{\tau}_i$,

$$\Phi = \Phi_{\text{ext}} - L_K[I_2(\varphi_2, \bar{\tau}_2) - I_1(\varphi_1, \bar{\tau}_1)]/2. \quad (4)$$

Taking into account flux quantization, we substitute $\varphi_2 = \varphi_1 - 2\pi\Phi$, resulting in an equation of two unknowns, φ_1 and Φ . Equation (4) is solved to obtain $\Phi_{\text{ext}}(\varphi_1, \Phi)$ and $I_{\text{SQUID}}(\varphi_1, \Phi) = I_1(\varphi_1, \bar{\tau}_1) + I_2(\varphi_1 - 2\pi\Phi, \bar{\tau}_2)$. After calculating Φ_{ext} and I_{SQUID} for every value of Φ and φ_1 , solutions are constrained using physical arguments: for each value of Φ_{ext} , the SQUID critical current is the maximum of I_{SQUID} . Similarly, the situation with only circulating currents (equivalent to the case where tunneling spectroscopy is measured) is obtained for $I_{\text{SQUID}} = 0$.

Fitting of our full model to the critical current of Fig. 2(b) resulted in effective transmissions $\bar{\tau}_1 = 0.69$ and $\bar{\tau}_2 = 0.92$, consistent with JJ1 having a larger electrodes separation than JJ2. The fit is shown in Fig. 3(a) (red line), with the computed φ_1 and φ_2 as a function of Φ_{ext} plotted in Fig. 3(b) (solid lines). Deviations from the simplified model are particularly relevant close to $\Phi_{\text{ext}} = \Phi_0/2$, where nonlinearities occur. The horizontal shift observed between the measured critical current of Fig. 2(b) and that numerically computed of Fig. 3(a) (indicated by the blue mark) is understood as due to the induced flux in the loop, driven by the large circulating current present in the measurement of Fig. 2(b) and absent when performing tunneling spectroscopy as in Fig. 2(c). The sensitivity of the calculated SQUID critical current on the choice of input parameters is presented in the Supplemental Material [32].

We now provide a quantitative understanding of the measured ABSs. Figure 3(c) shows the energy of the more transmissive ABSs extracted from Fig. 2(d) (blue dots) together with a fit of Eq. (1) that takes into account the nonlinear relation between Φ_{ext} and φ_1 represented in Fig. 3(b) (purple line). The fit of our full model finds excellent agreement with the measured ABS and results in $\tau_1 = 0.92$, among the highest values ever reported. The states with lower transmission visible in Fig. 2(b) were fit with transmission parameters 0.54 and 0.15. We contrast this with a fit using the simplified mapping between φ and Φ_{ext} (black dashed line), which does not take into account the presence of JJ2 and the loop kinetic inductance.

The low quality of this fit highlights how device complexities might result in severe distortions of the measured ABSs and should be properly accounted for.

In conclusion, we measured highly transmissive planar JJs embedded in an InAs/Al hybrid heterostructure. Thanks to a novel device design, we related the junction ABS spectrum to its CPR, finding remarkable agreement. Supercurrent gave an effective transmission $\bar{\tau}_1 = 0.69$, resulting in a forward-skewed CPR. On the other hand, tunneling spectroscopy provided a much richer description of the device, revealing sets of discrete ABSs populating the superconducting gap. We measured ABSs with almost unity transmission, well separated from other states and the continuum, and energy approaching zero for $\varphi_1 = \pi$. These levels are a promising starting point for engineering topological states either via phase biasing in multiterminal geometries [27,28] or in combination with small Zeeman fields [11,12]. Our Letter also highlights the complexities inherent in SQUID devices with ballistic junctions and large kinetic inductance and provides a framework for future studies.

This work was supported by Microsoft Corporation, the Danish National Research Foundation, and the Villum Foundation. F.N. acknowledges support from European Research Commission, Grant No. 804273. We thank A. Stern, E. Berg, F. Setiawan, A. Keselman, H. Pothier, L. Bretheau, and P. Scarlino for fruitful discussions.

*fni@ibm.zurich.com

†marcus@nbi.ku.dk

- [1] G. de Lange, B. van Heck, A. Bruno, D. J. van Woerkom, A. Geresdi, S. R. Plissard, E. P. A. M. Bakkers, A. R. Akhmerov, and L. DiCarlo, *Phys. Rev. Lett.* **115**, 127002 (2015).
- [2] T. W. Larsen, K. D. Petersson, F. Kuemmeth, T. S. Jespersen, P. Krogstrup, J. Nygård, and C. M. Marcus, *Phys. Rev. Lett.* **115**, 127001 (2015).
- [3] L. Casparis, M. R. Connolly, M. Kjaergaard, N. J. Pearson, A. Kringhøj, T. W. Larsen, F. Kuemmeth, T. Wang, C. Thomas, S. Gronin, G. C. Gardner, M. J. Manfra, C. M. Marcus, and K. D. Petersson, *Nat. Nanotechnol.* **13**, 915 (2018).
- [4] J. I.-J. Wang, D. Rodan-Legrain, L. Bretheau, D. L. Campbell, B. Kannan, D. Kim, M. Kjaergaard, P. Krantz, G. O. Samach, F. Yan, J. L. Yoder, K. Watanabe, T. Taniguchi, T. P. Orlando, S. Gustavsson, P. Jarillo-Herrero, and W. D. Oliver, *Nat. Nanotechnol.* **14**, 120 (2019).
- [5] M. Pita-Vidal, A. Bargerbos, C.-K. Yang, D. J. van Woerkom, W. Pfaff, N. Haider, P. Krogstrup, L. P. Kouwenhoven, G. de Lange, and A. Kou, *arXiv:1910.07978*.
- [6] S. Hart, H. Ren, M. Kosowsky, G. Ben-Shach, P. Leubner, H. Brüne, Christoph Buhmann, L. W. Molenkamp, B. I. Halperin, and A. Yacoby, *Nat. Phys.* **13**, 87 (2017).
- [7] D. B. Szombati, S. Nadj-Perge, D. Car, S. R. Plissard, E. P. A. M. Bakkers, and L. P. Kouwenhoven, *Nat. Phys.* **12**, 568 (2016).
- [8] E. M. Spanton, M. Deng, S. Vaitiekėnas, P. Krogstrup, J. Nygård, C. M. Marcus, and K. A. Moler, *Nat. Phys.* **13**, 1177 (2017).
- [9] A. Assouline, C. Feuillet-Palma, N. Bergeal, T. Zhang, A. Mottaghizadeh, A. Zimmers, E. Lhuillier, M. Eddrie, P. Atkinson, M. Aprili, and H. Aubin, *Nat. Commun.* **10**, 126 (2019).
- [10] W. Mayer, M. C. Dartailh, J. Yuan, K. S. Wickramasinghe, E. Rossi, and J. Shabani, *Nat. Commun.* **11**, 212 (2020).
- [11] M. Hell, M. Leijnse, and K. Flensberg, *Phys. Rev. Lett.* **118**, 107701 (2017).
- [12] F. Pientka, A. Keselman, E. Berg, A. Yacoby, A. Stern, and B. I. Halperin, *Phys. Rev. X* **7**, 021032 (2017).
- [13] A. Fornieri, A. M. Whiticar, F. Setiawan, E. Portoles, A. C. C. Drachmann, A. Keselman, S. Gronin, C. Thomas, T. Wang, R. Kallagher, G. C. Gardner, E. Berg, M. J. Manfra, A. Stern, C. M. Marcus, and F. Nichele, *Nature (London)* **569**, 89 (2019).
- [14] H. Ren, F. Pientka, S. Hart, A. T. Pierce, M. Kosowsky, L. Lunczer, R. Schlereth, B. Scharf, E. M. Hankiewicz, L. W. Molenkamp, B. I. Halperin, and A. Yacoby, *Nature (London)* **569**, 93 (2019).
- [15] W. Mayer, M. C. Dartailh, J. Yuan, K. S. Wickramasinghe, A. Matos-Abiague, I. Žutić, and J. Shabani, *arXiv:1906.01179*.
- [16] A. A. Golubov, M. Y. Kupriyanov, and E. Il'ichev, *Rev. Mod. Phys.* **76**, 411 (2004).
- [17] M. L. Della Rocca, M. Chauvin, B. Huard, H. Pothier, D. Esteve, and C. Urbina, *Phys. Rev. Lett.* **99**, 127005 (2007).
- [18] L. Bretheau, Ç. Ö. Girit, C. Urbina, D. Esteve, and H. Pothier, *Phys. Rev. X* **3**, 041034 (2013).
- [19] G. Nanda, J. L. Aguilera-Servin, P. Rakyta, A. Kormányos, R. Kleiner, D. Koelle, K. Watanabe, T. Taniguchi, L. M. K. Vandersypen, and S. Goswami, *Nano Lett.* **17**, 3396 (2017).
- [20] L. Bretheau, Ç. Girit, H. Pothier, D. Esteve, and C. Urbina, *Nature (London)* **499**, 312 (2013).
- [21] J.-D. Pillet, C. H. L. Quay, P. Morfin, C. Bena, A. L. Yeyati, and P. Joyez, *Nat. Phys.* **6**, 965 (2010).
- [22] L. Bretheau, J. I.-J. Wang, R. Pisoni, K. Watanabe, T. Taniguchi, and P. Jarillo-Herrero, *Nat. Phys.* **13**, 756 (2017).
- [23] W. Chang, V. E. Manucharyan, T. S. Jespersen, J. Nygård, and C. M. Marcus, *Phys. Rev. Lett.* **110**, 217005 (2013).
- [24] L. Tosi, C. Metzger, M. F. Goffman, C. Urbina, H. Pothier, S. Park, A. L. Yeyati, J. Nygård, and P. Krogstrup, *Phys. Rev. X* **9**, 011010 (2019).
- [25] A. Zazunov, V. S. Shumeiko, E. N. Bratus', J. Lantz, and G. Wendin, *Phys. Rev. Lett.* **90**, 087003 (2003).
- [26] C. Janvier, L. Tosi, L. Bretheau, Ç. Ö. Girit, M. Stern, P. Bertet, P. Joyez, D. Vion, D. Esteve, M. F. Goffman, H. Pothier, and C. Urbina, *Science* **349**, 1199 (2015).
- [27] B. van Heck, S. Mi, and A. R. Akhmerov, *Phys. Rev. B* **90**, 155450 (2014).

- [28] R.-P. Riwar, M. Houzet, J. S. Meyer, and Y. V. Nazarov, *Nat. Commun.* **7**, 11167 (2016).
- [29] N. Pankratova, H. Lee, R. Kuzmin, M. Vavilov, K. Wickramasinghe, W. Mayer, J. Yuan, J. Shabani, and V. E. Manucharyan, [arXiv:1812.06017](https://arxiv.org/abs/1812.06017).
- [30] J. Shabani, M. Kjaergaard, H. J. Suominen, Y. Kim, F. Nichele, K. Pakrouski, T. Stankevic, R. M. Lutchyn, P. Krogstrup, R. Feidenhans'l, S. Kraemer, C. Nayak, M. Troyer, C. M. Marcus, and C. J. Palmstrøm, *Phys. Rev. B* **93**, 155402 (2016).
- [31] M. Kjaergaard, F. Nichele, H. J. Suominen, M. P. Nowak, M. Wimmer, A. R. Akhmerov, J. A. Folk, K. Flensberg, J. Shabani, C. J. Palmstrøm, and C. M. Marcus, *Nat. Commun.* **7**, 12841 (2016).
- [32] See Supplemental Material at <http://link.aps.org/supplemental/10.1103/PhysRevLett.124.226801> for further experimental information, additional measurements, and a more detailed analysis, which include Refs. [33–35].
- [33] A. J. Annunziata, D. F. Santavicca, L. Frunzio, G. Catelani, M. J. Rooks, A. Frydman, and D. E. Prober, *Nanotechnology* **21**, 445202 (2010).
- [34] F. Setiawan, C.-T. Wu, and K. Levin, *Phys. Rev. B* **99**, 174511 (2019).
- [35] M. Tinkham, *Introduction to Superconductivity* (Dover Publications, New York, 2004).
- [36] M. Kjaergaard, H. J. Suominen, M. P. Nowak, A. R. Akhmerov, J. Shabani, C. J. Palmstrøm, F. Nichele, and C. M. Marcus, *Phys. Rev. Applied* **7**, 034029 (2017).
- [37] C. W. J. Beenakker and H. van Houten, *Phys. Rev. Lett.* **66**, 3056 (1991).
- [38] H. J. Suominen, M. Kjaergaard, A. R. Hamilton, J. Shabani, C. J. Palmstrøm, C. M. Marcus, and F. Nichele, *Phys. Rev. Lett.* **119**, 176805 (2017).
- [39] First, the critical current was numerically identified as the I_2 value at which $dV_2/dI_2 = 10 \Omega$. The slowly varying curvature due to Fraunhofer interference was then numerically subtracted from the data.